Title	Audio frequency in vivo optical coherence elastography
Author(s)	Adie, Steven G.; Kennedy, Brendan F.; Armstrong, Julian J.; Alexandrov, Sergey; Sampson, David
Publication Date	2009-05-06
Publication Information	Adie, Steven G., Kennedy, Brendan F., Armstrong, Julian J., Alexandrov, Sergey A., & Sampson, David D. (2009). Audio frequencyin vivooptical coherence elastography. Physics in Medicine and Biology, 54(10), 3129-3139. doi: 10.1088/0031-9155/54/10/011
Publisher	IOP Publishing
Link to publisher's version	https://doi.org/10.1088/0031-9155/54/10/011
Item record	http://hdl.handle.net/10379/17119
DOI	http://dx.doi.org/10.1088/0031-9155/54/10/011

IOP PUBLISHING PHYSICS IN MEDICINE AND BIOLOGY

Phys. Med. Biol. **54** (2009) 3129–3139 doi:10.1088/0031-9155/54/10/011

Audio frequency *in vivo* optical coherence elastography

Steven G Adie[1], Brendan F Kennedy, Julian J Armstrong, Sergey A Alexandrov and David D Sampson

Optical+Biomedical Engineering Laboratory (OBEL), School of Electrical, Electronic & Computer Engineering, The University of Western Australia, 35 Stirling Highway, Crawley, Western Australia 6009, Australia

E-mail: dsampson@ee.uwa.edu.au

Received 1 December 2008, in final form 3 April 2009
Published 6 May 2009
Online at stacks.iop.org/PMB/54/3129

Abstract

We present a new approach to optical coherence elastography (OCE), which probes the local elastic properties of tissue by using optical coherence tomography to measure the effect of an applied stimulus in the audio frequency range. We describe the approach, based on analysis of the Bessel frequency spectrum of the interferometric signal detected from scatterers undergoing periodic motion in response to an applied stimulus. We present quantitative results of sub-micron excitation at 820 Hz in a layered phantom and the first such measurements in human skin *in vivo*.

(Some figures in this article are in colour only in the electronic version)

1. Introduction

For centuries physicians have used palpation, i.e. sensing stiffness through touch, as an indicator of abnormal or diseased tissue (Greenleaf *et al* 2003, Fatemi *et al* 2003). For example, cancer is often detected via the increased hardness or stiffness of a tumour compared to the surrounding tissue (Fatemi *et al* 2003, Gao *et al* 1996). Young's modulus (the ratio of stress to strain) of breast tumours may vary from that of the surrounding tissue by up to a factor of 90, and may vary by up to four orders of magnitude in soft tissues (Greenleaf *et al* 2003, Sarvazyan *et al* 1998). The ability to move beyond the subjectivity and low resolution of palpation to the quantitative and non-invasive imaging of the elastic properties of tissue should provide an important advance in diagnostic capability.

The term elastography refers to the measurement and imaging of the elastic properties of tissue. Elastography has been performed with magnetic resonance imaging (MRI), with ultrasound imaging and with optical methods (Greenleaf *et al* 2003, Fatemi *et al* 2003, Parker

[1] Present address: Biophotonics Imaging Laboratory, Beckman Institute for Advanced Science and Technology, University of Illinois at Urbana-Champaign, 405 North Mathews Avenue, Urbana, IL 61801, USA.

et al 1996, Gao *et al* 1996). The elastic properties of the medium so determined are subject to the spatial resolution and noise limitations of the respective parent modalities, as well as to other practical limitations such as gross tissue motion artefact and the acoustic propagation loss (Parker *et al* 2005). Optical coherence tomography (OCT) has superior spatial resolution to the aforementioned modalities up to its penetration depth, typically a few millimetres; thus, optical coherence elastography (OCE) benefits from the superior spatial resolution of its parent modality.

The majority of OCE schemes reported to date have been based on speckle-tracking techniques and have employed predominantly quasi-static mechanical loading of tissue to quantitatively assess local tissue motion (Ko *et al* 2006, Rogowska *et al* 2004, Chan *et al* 2004, Schmitt 1998). One study has utilized non-contact acoustic excitation (20 kHz) with the objective of enhancing OCT contrast (Edney and Walsh 2001) but did not demonstrate quantitative elastography. More recently, techniques have been developed based on phase-sensitive spectral-domain OCT (Liang *et al* 2008, Wang *et al* 2006). However, in these techniques, the excitation frequency has been limited to 20 Hz or less.

In this paper, we present a new approach to OCE suitable for quantitative measurement of tissue elastic properties in the hundred hertz to kilohertz frequency range. This frequency range, which has been the target range for elastography based on other imaging modalities, matches the typical frequency response range of many biological tissues (Fatemi and Greenleaf 1998, Parker *et al* 1990, Potts *et al* 1983). Section 2 describes the theory behind our approach. Section 3 describes the experimental system and data analysis. Section 4 presents experimental results and discussion of dynamic OCE measurements at 820 Hz, in both a three-layer phantom and human skin tissue *in vivo*. Section 5 reports the main conclusions and implications of the work.

2. Theory

Consider an interferometric signal generated by the combination of a reference light beam and light backscattered from scatterers undergoing harmonic displacement along the optical (z) axis in response to an external excitation, all light having been derived from the same low-coherence source. At frequencies of up to several kHz (with the corresponding sound wavelength $\Lambda \sim 1$ m), scatterers in a medium of typical thickness $\sim$1 mm can be expected to move in phase with each other. The dynamic interferometric signal amplitude of interest depends not only on the scatterer's vibration amplitude but also on the quasi-static phase of the interferometer, which, in turn, is governed by the precise differential axial position of the scatterer relative to the reference path in the interferometer. This undesired dependence of the dynamic displacement on the quasi-static displacement is generally known as interferometric signal fading (Udd 1991). It can be overcome by various means, including by polarization-based optical quadrature detection (Zhao *et al* 2002). In such a case, the detected photocurrents in the orthogonal polarization channels, denoted by the subscripts 1 and 2, can be described by

$$i_1(z,t) = 2\rho\sqrt{I_R I_S}\cos[\phi_{DC} + \phi_S \sin(2\pi\Omega t)] \tag{1}$$

$$i_2(z,t) = 2\rho\sqrt{I_R I_S}\sin[\phi_{DC} + \phi_S \sin(2\pi\Omega t)], \tag{2}$$

where Ω is the frequency of the harmonic excitation, I_S and I_R are the sample and reference optical intensities, respectively, ϕ_{DC} is the quasi-static interferometric phase (modulo 2π) governed by the mean axial position of the scatterer, $\phi_s = \frac{4\pi}{\lambda} d(z,\Omega)$, where λ is the

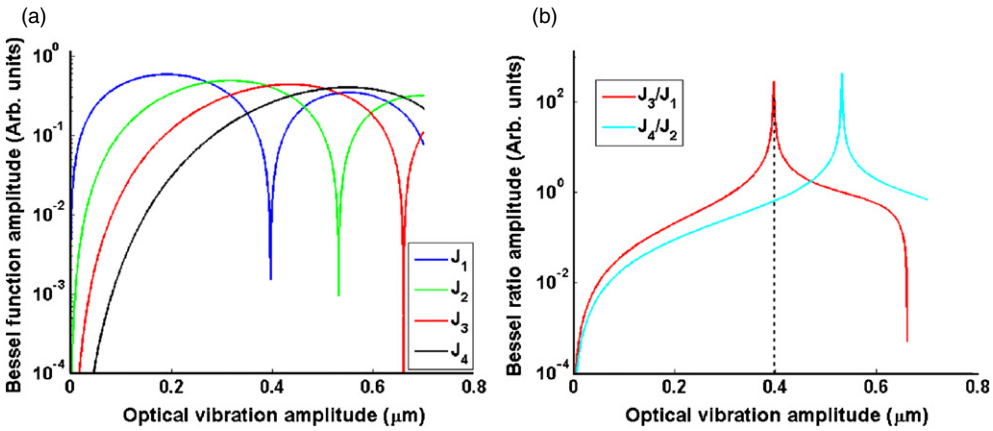

Figure 1. (a) Amplitude of Bessel functions J_1–J_4 versus vibration amplitude; (b) J_3/J_1 and J_4/J_2 versus vibration amplitude. The dashed line denotes the asymptote.

mean optical wavelength in the medium, d is the local, generally frequency-dependent, axial displacement amplitude, and ρ is the detector responsivity. It is readily seen from (1) and (2) that the value of ϕ_{DC} alters the detected signal and therefore the apparent dynamic signal amplitude. Equations (1) and (2) may be expanded as a series of Bessel functions (Udd 1991, Sasaki and Okazaki 1986), resulting in the following:

$$i_1(z,t) = 2\rho\sqrt{I_R I_S}\left\{\cos\phi_{DC}\left[J_0(\phi_S) + 2\sum_{n=1}^{\infty} J_{2n}(\phi_S)\cos(4\pi n\Omega t)\right] - \sin\phi_{DC}\left[2\sum_{n=0}^{\infty} J_{2n+1}(\phi_S)\sin(2\pi(2n+1)\Omega t)\right]\right\} \tag{3}$$

$$i_2(z,t) = 2\rho\sqrt{I_R I_S}\left\{\sin\phi_{DC}\left[J_0(\phi_S) + 2\sum_{n=1}^{\infty} J_{2n}(\phi_S)\cos(4\pi n\Omega t)\right] + \cos\phi_{DC}\left[2\sum_{n=0}^{\infty} J_{2n+1}(\phi_S)\sin(2\pi(2n+1)\Omega t)\right]\right\}, \tag{4}$$

where J_n is the nth-order Bessel function of the first kind. Choosing for example $\phi_{DC} = \pi/2$ in (3) and (4), it is clear that the even harmonics of the signal fade in channel 1 and the converse is true in channel 2. Thus, to account for the effect of signal fading, the quadrature channels may be combined incoherently, i.e. by calculating the sum of the envelopes squared followed by a square root operation. Having accounted for signal fading, the amplitude of the even harmonics is proportional to J_{2n}, and that of the odd harmonics to J_{2n+1}.

The objective of the OCE scheme presented here is to determine from an interferometric measurement of ϕ_S the amplitude of the dynamic axial displacement, i.e. the vibration amplitude of the scatterer. This has been achieved through the piecewise mapping of the measured ratios of Bessel harmonic terms to vibration amplitude based on (3) and (4). Figure 1 displays the dependence of these terms as a function of vibration amplitude.

In our approach, the (full-fringed) interferometric signal is recorded in two dimensions (an OCT B-scan), and the quadrature signals are filtered and incoherently combined at Ω,

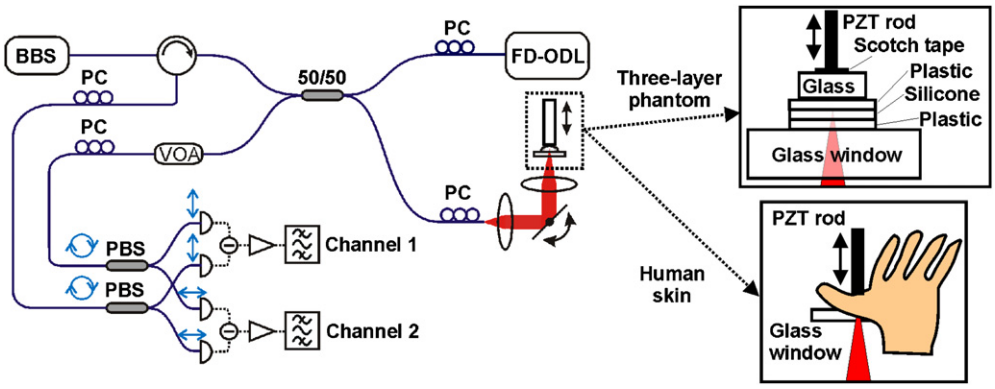

Figure 2. Schematic of the OCT system employing balanced optical quadrature detection. The insets show the phantom and *in vivo* experimental geometries. BBS: broadband source, PC: polarization controller, FD-ODL: frequency-domain optical delay line, VOA: variable optical attenuator and PBS: (fibre-based) polarizing beamsplitter.

2Ω, 3Ω and 4Ω. The theoretical values of the ratio J_3/J_1 are used to map the experimentally measured value of the ratio to vibration amplitude, as shown in figure 1(b). By also computing the ratio J_4/J_2, the unambiguous range of operation can be extended beyond the asymptotic point at approximately $\lambda/3$ by using it to identify on which side of the asymptotic value lies the measured value of the ratio J_3/J_1. At a mean wavelength of $\lambda = 1.3$ μm, this permits the measurement of vibration amplitudes of up to about 0.65 μm, corresponding to the second zero of J_3. Note that the measured vibration amplitude is the product of the physical vibration amplitude and the refractive index of the scattering medium, which we term 'optical vibration amplitude' for clarity.

3. Experimental method and data analysis

A schematic of the experimental fibre-based, time-domain OCT system utilizing balanced optical quadrature detection is presented in figure 2. The broadband superluminescent source emitted light at a mean wavelength of 1334 nm with a near-Gaussian spectrum and 3 dB bandwidth of 42 nm, launching 7.75 mW of polarized light into the OCT system. After passing through a circulator, the light was split by a 50/50 coupler into the sample and reference arms. The reference arm comprised a frequency-domain optical delay line utilizing a blazed grating with 400 lines mm^{-1} and a blaze angle of 13.9°. In the sample arm, a triplet lens ($f = 30$ mm) was used to focus the beam through a glass window that provided a rigid platform upon which the samples were placed and provided a lateral resolution of 15.3 μm. The sensitivity of the system, using a glass–air interface at normal incidence as a calibrated reflector, was measured to be 113 dB. Dynamic compression was applied to the sample, as indicated in figure 2 (inset), with a piezoelectric rod actuator operated at a frequency of 820 Hz. The stiffness of the actuator was 4 N μm^{-1}.

After recombination, the light was split into orthogonal polarization channels by fibre-based polarization beam splitters with >27 dB extinction ratio. Balanced InGaAs photodetectors, providing a common-mode rejection ratio of 25 dB, were used to detect the polarization channels.

The channels were balanced by monitoring the signals generated by the glass–air interface of the sample arm window while adjusting the polarization controllers and the variable optical

attenuator. Signals in exact quadrature (zero mean, equal amplitudes and 90° phase difference) produced a circular pattern on an oscilloscope operated in the XY mode.

The FD-ODL was operated at one of two galvanometer pivot offsets, according to whether the sample was vibrated or not. Without applied vibration, conventional OCT images were acquired with the galvanometer pivot offset to generate a carrier frequency of 1150 Hz (Zvyagin *et al* 2003). With applied vibration, the FD-ODL was operated on-pivot and the carrier frequency was, in effect, generated by the vibration of sample scatterers. On-pivot operation has the advantage of reducing the impact of the phase noise (e.g. arising from the jitter of the galvanometer) and maximizing the vibration sensitivity of the system, which we measured to be 50 nm. Phase noise introduced by jitter of the galvanometer would directly contribute to the vibration harmonics and, therefore, could not be removed by filtering. As the vibration amplitude is determined through measurement of the ratio between vibration harmonics, the minimum detectable vibration would increase.

The data acquisition rate was limited by the requirement that the vibration signal harmonic spectra do not overlap each other, which in turn restricts the OCT electrical signal bandwidth to a fraction of the vibration frequency. We define $a = \Omega/\Delta f$ as the ratio of the vibration frequency to the electrical bandwidth Δf and required $a \geqslant 4$ to ensure adequate separation (and detection) of the harmonic spectra. The A-scan velocity, v, can be related to Δf (Sampson and Hillman 2004) and, therefore, the velocity must satisfy

$$v \leqslant \frac{1}{4}\frac{\pi}{4\ln 2} l_c \Omega. \tag{5}$$

Higher vibration frequencies, therefore, permit higher acquisition rates. In this study, a conservative A-scan frequency of 0.26 Hz was used, leading to an electrical signal bandwidth of 130 Hz, which resulted in $a \approx 6$.

To test the approach, we constructed a three-layer phantom comprising a readily compressible layer (translucent silicone sealant) sandwiched between two stiffer, less compliant layers (translucent polypropylene plastic) of near-identical elastic properties. All three layers were approximately 0.3 mm thick and ~20 mm square. The piezoelectric rod actuator (~2 mm diameter rod) was coupled to the phantom via a glass layer (~10 mm square piece cut from a microscope slide) to facilitate application of uniform pressure to the phantom. The glass and actuator were aligned to the centre of the phantom, and the rod was collinear with the optical beam, as shown in the inset of figure 2. For the *in vivo* measurements, the actuator was coupled directly to the human skin, without the use of an intermediate glass layer. OCE images were recorded for a range of piezoelectric actuator drive voltages.

Both OCT (no vibration) and OCE measurements were made on the phantom and on human skin. All images to be presented in the next section were generated from single B-scans. The OCE images contain fewer A-scans and were acquired over a smaller field-of-view than the OCT images in order to limit the total acquisition time and, therefore, minimize both sample motion artefact and boundary effects between OCT and OCE images. Naturally, these effects were more prominent in the *in vivo* measurements.

The interferometric signal in each channel was 12-bit digitized at a rate of 0.6 MSamples s^{-1} with a 12-bit analogue-to-digital converter. Analysis of the recorded signals was carried out in post-processing. Intensity images were calculated for four separate harmonic frequencies by applying bandpass filters centred at Ω, 2Ω, 3Ω and 4Ω (producing, in total, eight images from the two channels). The signals forming these images were then separately demodulated utilizing the Hilbert transform, to extract the vibration harmonics, and the resulting orthogonal envelopes at each frequency in each channel were incoherently combined to account for signal fading. The resulting four images were used to produce an image of the local vibration amplitude using the ratio J_3/J_1, as previously described.

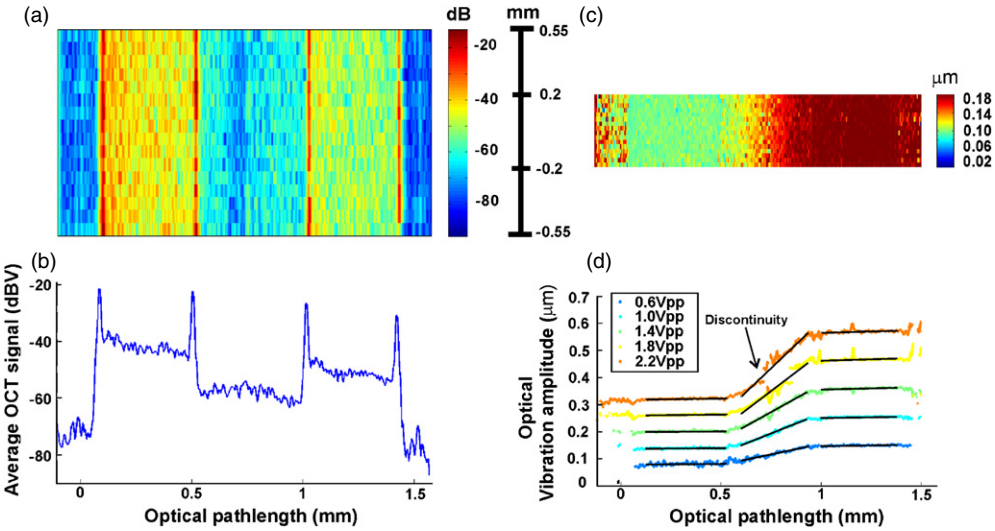

Figure 3. OCT and OCE images and derived plots for the three-layer phantom: (a) OCT image (no applied vibration), dimensions: 1.6 by 1.1 mm; (b) average A-scan derived from (a); (c) OCE image for actuator drive voltage of 1.0 V p-p, dimensions: 1.6 by 0.4 mm, and (d) average vibration amplitude for indicated actuator drive voltages (black superimposed lines are linear fits). For all parts of the figure, the optical beam was incident from the left and vibration was applied from the right.

When the signal-to-noise ratio (SNR) of the harmonic signals corresponding to J_3 or J_1 is low, it was found that calculation of the vibration amplitude from their ratio is prone to error. Notably, in the case of zero vibration amplitude, the ratio J_3/J_1 is simply determined by the spectral noise floor of the system. To determine the validity of the computed vibration amplitude, two conditions based on the SNR of the detected harmonics were applied. The measured signal was considered valid when the SNRs of both J_1 and J_3 were at least 15 dB, or if the SNR of J_1 was at least 30 dB. The SNR of each harmonic was calculated relative to the noise floor of the spectrum in its vicinity, in order to account for any spectral dependence. The spectral noise floor was calculated as the average of the bandpass filtered signals centred at $J_m - 3\Delta f$ and $J_m + 3\Delta f$, where $m = 1$ or 3 and Δf is the signal bandwidth of the fundamental J_1. The spectral noise floor varied depending on sample reflectivity but was typically measured to be 30 dB below the signal for skin measurements.

4. Results and discussion

The OCT and OCE images of the three-layer phantom are presented in figure 3. Figure 3(a) shows the OCT image (64 A-scans over a lateral range of 1.1 mm) and the average A-scan is shown in figure 3(b). Figure 3(c) shows the OCE image (16 A-scans over the central 0.4 mm part of the OCT lateral range). OCE images were recorded for a range of piezoelectric actuator drive voltages between 0.6 and 2.2 V peak-to-peak. Both the depth dimension and vibration amplitude are products of their respective physical dimension and refractive index, as described in section 2.

The OCT image and average A-scan clearly show the three layers of the phantom. In the first layer, a higher optical signal is evident than that in the third layer, even though both

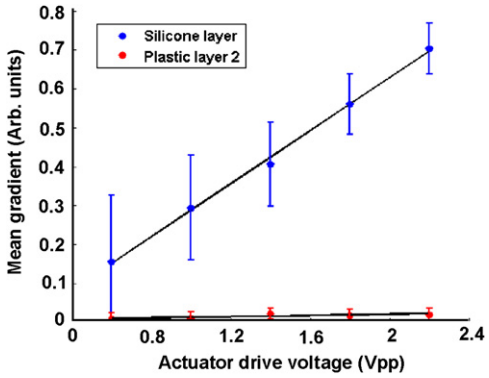

Figure 4. Gradient of linear fits to the traces in figure 3(d).

layers are made from identical material, because of the extinction upon propagation through the turbid medium.

The average vibration amplitudes in figure 3(d) do not vary significantly with depth within the first and third layers and show an approximately linear variation with depth in the silicone (middle) layer. This behaviour is expected since the silicone is much more compressible than the plastic. In contrast to the OCT signal, the average vibration amplitude is greatest in the third layer, as expected, since it is proximal to the applied pressure and distal to the sample arm window. The finite vibration amplitude of the first layer and its increase with actuator drive voltage indicates that the sample arm glass window is not perfectly rigid.

The actual vibration amplitude in a given layer of the phantom is related to the strain, defined as $\Delta L/L_0$, where L_0 is the thickness of the layer. The gradient of the vibration amplitude is equal to the total strain in the layer less the strain due to the pressure when the actuator is at rest. Therefore, in effect, we measure the amplitude of the dynamic differential strain in each layer. Constant vibration amplitude is observed in the first and third layers indicating bulk motion of the layer, for which the dynamic differential strain is approximately zero. In contrast, a linear variation in the strain is observed within the silicone layer (see linear fits in figure 3(d)), indicating that it is relatively more compressible than the plastic layers and, therefore, has a lower dynamic Young's modulus (at 820 Hz). The Young's modulus E is defined by

$$E = \frac{\text{Stress}}{\text{Strain}} = \frac{F/A_0}{\Delta L/L_0}, \tag{6}$$

where the stress is defined as the force, F, applied to an object over the cross-sectional area, A_0.

Figure 4 plots the gradient of the optical vibration amplitude versus optical pathlength against actuator drive voltage. The plot demonstrates a linear relationship between the dynamic differential strain in the silicone layer and the drive voltage. Assuming that the stress produced by the actuator has the expected linear dependence on drive voltage, this linear relationship indicates that the compression of the silicone layer is elastic, i.e. in the linear region of the material's stress–strain curve. The gradient of the optical vibration amplitude versus optical pathlength against actuator drive voltage in the second plastic layer is also plotted in figure 4. A linear fit of the gradient in both layers is presented. The ratio of the dynamic differential strain between the silicone and plastic layers (average of the dynamic differential strain in the two plastic layers) is calculated to determine their relative elastic properties. Using (6), it is

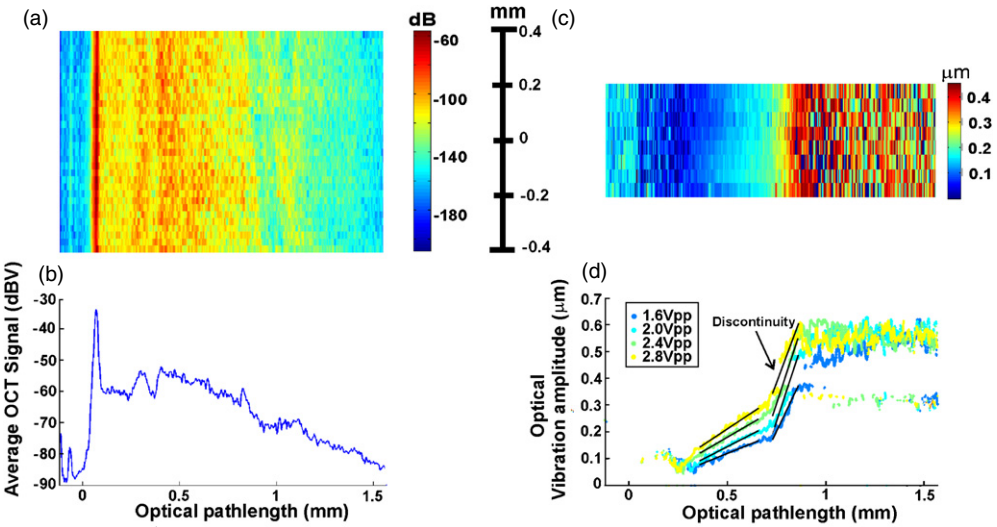

Figure 5. OCT and OCE images and derived data for human skin *in vivo*: (a) OCT image (without applied vibration), dimensions: 1.6 by 0.8 mm; (b) average A-scan; (c) vibration amplitude image at an actuator drive voltage of 2.4 V p-p, dimensions: 1.6 by 0.4 mm, and (d) average vibration amplitude for various actuator drive voltages (black superimposed lines are linear fits). For all parts of the figure, the optical beam was incident from the left and the excitation was applied from the right.

calculated that the dynamic (820 Hz) Young's modulus of the plastic, based on these five data points, is 30 ± 12 times greater than that of the silicone, assuming equal stress in each layer. It should be noted that the first plastic layer also responds approximately linearly (not plotted here), due to residual bulk motion of the sample, indicating that it is not rigidly coupled to the glass window.

Figure 5 presents results of *in vivo* measurements of human skin obtained by compressing the 'webbing' between the thumb and index finger between the actuator rod and the sample-arm window. The OCT image in figure 5(a) consists of 32 A-scans taken over a lateral scan range of 0.8 mm. The lateral spacing is relatively large compared to the lateral resolution in order to obtain both reasonable field of view and acquisition time given the low A-scan rate. The vibration amplitude measurement in figure 5(c) consisted of eight A-scans centred at the same lateral position, but over a 0.4 mm range.

A relatively uniform signal is in evidence from the skin's surface to a depth of 0.2 mm, distinguishable in both the OCT image (figure 5(a)) and the average A-scan (figure 5(b)), which corresponds to a layer with low vibration amplitude in figure 5(d). This layer is attributed to the stratum corneum and is expected to display negligible vibration amplitude due to its tight coupling to the rigid glass window and its low compressibility.

Below the expected extent of the stratum corneum, $z = 0.2$ mm, the OCT image does not show any clear boundary between skin layers until a depth of approximately 0.85 mm. In contrast, all the vibration amplitude traces in figure 5(d) show a distinct difference in slope at about 0.65 mm. This change in slope indicates the presence of two layers of different compressibility, with the deeper layer (with greater slope) being relatively more compressible. These layers are attributed to the epidermis and dermis, respectively, which are known to have distinct elastic properties (Agache and Humbert 2004).

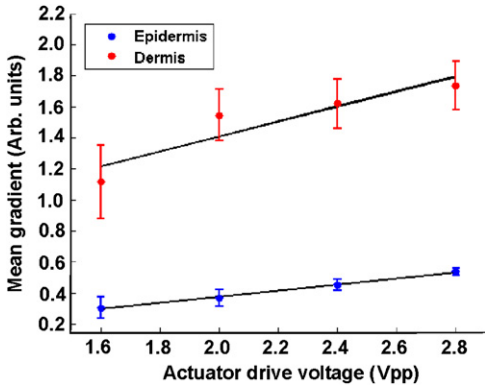

Figure 6. Gradient of linear fits to traces in figure 5(d).

The discontinuity evident in the vibration amplitude versus pathlength curves of figures 3(d) (1.8 V p-p and 2.2 V p-p traces) and 5(d) is an artefact occurring at the intersection of the two calibration regions in the J_3/J_1 curve plotted in figure 1(b) (when the vibration amplitude is approximately $\lambda/3$).

The slopes of the vibration amplitude versus pathlength within the epidermis and dermis were estimated by performing linear fits to each region, as shown in figure 5(d). Figure 6 plots the gradients of these linear fits versus actuator drive voltage. A highly linear response is observed for the epidermis indicating that the response is elastic. In the same manner as for the epidermis, the resulting linear relationship suggests that the response of the dermis is also elastic. From the measurements in figure 6, it is calculated that the epidermis has a Young's modulus 3.7 ± 0.2 times greater than the dermis, assuming equal stress in the epidermis and dermis.

The dynamic OCE method put forward here naturally detects the axial motion of scatterers. Accordingly, our experimental geometry was designed so that, in each case, the actuator applied even pressure to the sample coaxially with the optical beam. Further work is required to establish the feasibility of accurately detecting vibration amplitude in the presence of lateral scatterer motion, such as when shear waves are excited.

The *in vivo* application of dynamic OCE is limited by two factors: acquisition speed and the need for coaxial optical beam and vibration excitation, with the light source and excitation source incident from the same direction. In our acquisition scheme, point-by-point acquisition with TD-OCT is limited by the requirement for adequate frequency separation between the OCT signal spectra at each of the vibration harmonics, each of which broadens as the acquisition rate increases. At the present A-scan rate of 0.26 Hz, the measurements are more susceptible than desirable to sample motion artefacts. Acquisition time can be improved by an excitation frequency in the kHz regime and beyond, for example, through the use of ultrasonic transducers (Fatemi and Greenleaf 1998). Potentially, both issues could be addressed by use of an ultrasonic transducer array such that a focussed ultrasound beam excites the sample in the 1–10 kHz range. Alternatively, the use of phase-sensitive spectral-domain OCT (Wang *et al* 2006, 2007) could be used with a high-speed A-scan rate and slow lateral scan to observe a given lateral location over several oscillation cycles. However, to date, this method has not been utilized for *in vivo* measurements or measurements at vibration frequencies beyond about 20 Hz.

Quantitative measurements of tissue elastic moduli require the local stress field to be known, which is a function of the force applied and the properties of any intervening structures including tissues. Such moduli are also dependent on tissue viscosity at low frequencies, and excitation at above 100 Hz may prove an advantage in this regard, avoiding this potential ambiguity. A combination of careful calibration and modelling, and comparison with gold standards, will be required to accurately measure absolute elastic properties. This will be the focus of future work.

5. Conclusions

In conclusion, we have presented a new dynamic OCE method suited to differential strain measurement based on sub-micron displacements at frequencies in the 100 Hz to 10 kHz regime. Using the method, it was possible to distinguish the differences in elasticity at 820 Hz between the layers in a three-layer phantom. The first reported quantitative *in vivo* OCE measurements of human skin presented here demonstrated varying elastic responses between layers. The minimum detectable vibration amplitude was measured to be 50 nm, and the maximum measured vibration amplitude was 0.65 μm.

The approach could readily perform high spatial-resolution measurements of the response of samples by scanning the excitation frequency over the audio range, which has the potential to detect weak resonances. Such measurements of tissue response, at single or multiple excitation frequencies, could potentially aid in the diagnosis of a range of medical conditions, including tumours and arterial plaques.

References

Agache P and Humbert P 2004 *Measuring the Skin: Non-Invasive Investigations, Physiology, Normal Constants* (Berlin: Springer)

Chan R C, Chau A H, Karl W C, Nadkarni S, Khalil A S, Iftimia N, Shishkov M, Tearney G J, Kaazempur-Mofrad M R and Bouma B E 2004 OCT-based arterial elastography: robust estimation exploiting tissue biomechanics *Opt. Express* **12** 4558–72

Edney P A and Walsh J T 2001 Acoustic modulation and photon-phonon scattering in optical coherence tomography *Appl. Opt.* **40** 6381–8

Fatemi M and Greenleaf J F 1998 Ultrasound-stimulated vibro-acoustic spectrography *Science* **280** 82–5

Fatemi M, Manduca A and Greenleaf J F 2003 Imaging elastic properties of biological tissues by low-frequency harmonic vibration *Proc. IEEE* **91** 1503–19

Gao L, Parker K J, Lerner R M and Levinson S F 1996 Imaging of the elastic properties of tissue—a review *Ultrasound Med. Biol.* **22** 959–77

Greenleaf J F, Fatemi M and Insana M 2003 Selected methods for imaging elastic properties of biological tissues *Annu. Rev. Biomed. Eng.* **5** 57–78

Ko H J, Tan W, Stack R and Boppart S A 2006 Optical coherence elastography of engineered and developing tissue *Tissue Eng.* **12** 63–73

Liang X, Oldenburg A L, Crecea V, Chaney E J and Boppart S A 2008 Optical micro-scale mapping of dynamic biomechanical tissue properties *Opt. Express* **16** 11052–65

Parker K J, Gao L, Lerner R M and Levinson S F 1996 Techniques for elastic imaging: a review *IEEE Eng. Med. Biol. Mag.* **15** 52–9

Parker K J, Huang S R, Musulin R A and Lerner R M 1990 Tissue response to mechanical vibrations for 'sonoelasticity imaging' *Ultrasound Med. Biol.* **16** 241–6

Parker K J, Taylor L S, Gracewski S and Rubens D J 2005 A unified view of imaging the elastic properties of tissue *J. Acoust. Soc. Am.* **117** 2705–12

Potts R O, Chrisman D A and Buras E M 1983 The mechanical properties of human skin *in vivo J. Biomech.* **16** 365–72

Rogowska J, Patel N A, Fujimoto J G and Brezinski M E 2004 Optical coherence tomographic elastography technique for measuring deformation and strain of atherosclerotic tissues *Heart* **90** 556–62

Sampson D D and Hillman T R 2004 *Lasers and Current Optical Techniques in Biology* (Cambridge: Royal Society of Chemistry) chapter 17, pp 481–571

Sarvazyan A P, Rudenko O V, Swanson S D, Fowlkes J B and Emelianov S Y 1998 Shear wave elasticity imaging: a new ultrasonic technology of medical diagnostics *Ultrasound Med. Biol.* **24** 1419–35

Sasaki O and Okazaki H 1986 Sinusoidal phase modulating interferometry for surface profile measurement *Appl. Opt.* **25** 3137–40

Schmitt J M 1998 OCT elastography: imaging microscopic deformation and strain of tissue *Opt. Express* **3** 199–211

Udd E 1991 *Fiber Optic Sensors: An Introduction for Engineers and Scientists* (New York: Wiley)

Wang R K K, Kirkpatrick S and Hinds M 2007 Phase-sensitive optical coherence elastography for mapping tissue microstrains in real time *Appl. Phys. Lett.* **90** 164105

Wang R K K, Ma Z H and Kirkpatrick S J 2006 Tissue Doppler optical coherence elastography for real time strain rate and strain mapping of soft tissue *Appl. Phys. Lett.* **89** 144103

Zhao Y H, Chen Z P, Ding Z H, Ren H W and Nelson J S 2002 Real-time phase-resolved functional optical coherence tomography by use of optical Hilbert transformation *Opt. Lett.* **27** 98–100

Zvyagin A V, Smith E D J and Sampson D D 2003 Delay and dispersion characteristics of a frequency-domain optical delay line for scanning interferometry *J. Opt. Soc. Am.* A **20** 333–41